

Optimized traverse planning for future polar prospectors based on lunar topography



E.J. Speyerer^{a,*}, S.J. Lawrence^a, J.D. Stopar^a, P. Gläser^b, M.S. Robinson^a, B.L. Jolliff^c

^aSchool of Earth and Space Exploration, Arizona State University, Tempe, AZ 85281, USA

^bDepartment of Geodesy and Geoinformation Science, Technical University Berlin, Berlin, Germany

^cDepartment of Earth and Planetary Sciences, Washington University in St. Louis, St. Louis, MO 63130, USA

ARTICLE INFO

Article history:

Received 7 July 2015

Revised 29 February 2016

Accepted 9 March 2016

Available online 21 March 2016

Keywords:

Moon

Terrestrial planets

Data reduction techniques

ABSTRACT

To fully understand the extensive collection of remotely sensed polar observations by the Lunar Reconnaissance Orbiter and other recent lunar missions, we must acquire an array of ground-truth measurements. A polar rover can sample and assay potential polar resources both laterally and at shallow depths. To identify ideal, least-energy traverses for such a polar prospecting mission, we developed a traverse planning tool, called *R-Traversal*, using a fundamental wheel–regolith interaction model and datasets from the Lunar Reconnaissance Orbiter Camera, Lunar Orbiter Laser Altimeter, and Diviner Lunar Radiometer Experiment. Using the terramechanics model, we identified least-energy traverses at the 20 m scale around Shackleton crater and located one traverse plan that enables the rover to remain illuminated for 94.4% of the lunar year. By incorporating this path planning tool during mission planning, the feasibility of such a mission can be quantified.

© 2016 Elsevier Inc. All rights reserved.

1. Introduction

Recent lunar missions provide the planetary science community with vast amounts of new data enabling important insights into the geology and evolution of the Moon on a global scale. Remotely sensed observations of the polar regions reveal the spatial and temporal distribution of persistently illuminated regions and broad-scale evidence for volatiles captured in cold traps (Bussey et al., 1999; Feldman, 1998; Feldman et al., 2000; Colaprete et al., 2010; Mitrofanov et al., 2010; Speyerer and Robinson, 2013; Gläser et al., 2014). In-situ resource utilization (ISRU) of these volatiles has the potential to transform these regions into fueling stations for future lunar missions as well as create a sustainable architecture for the exploration of the Solar System (Spudis and Lavoie, 2010; Spudis 2011). However, there are still many questions regarding the chemistry and extent of these cold-trapped resources.

A polar rover can address many outstanding questions by sampling a series of sites to assay resources not only along the surface, but also at shallow depths (~1 m). These ground measurements are essential to calibrate remotely sensed observations and provide first order estimates of *tonnage* and *grade* of any resource deposit. NASA's Human Exploration and Operations Mission Directorate's

proposed Resource Prospector mission (Andrews et al., 2014) aims to have a rover traverse across an area near the lunar South Pole. Along the traverse, the selected payload would detect and map volatile concentrations while examining an array of small permanently shaded regions (PSRs) of various sizes, locations, and types (i.e., inside of an impact crater or inside a local shaded depression not associated with an impact event) as well as areas that receive limited solar illumination. These measurements will help determine the form of volatile-element deposits and how concentrations and compositions vary from location to location within a PSR and from one PSR to another at the surface and at depth. Such measurements are needed to interpret and maximize the return on data from neutron spectrometer measurements of hydrogen (Feldman, 1998; Feldman et al., 2000; Mitrofanov et al., 2010) and interpretations and inferences drawn from the results of the LCROSS mission (e.g., Colaprete et al., 2010; Hurley et al., 2012). By tying these with remote measurements from LRO and other recent missions, we could select potential resource-rich sites for future exploration missions. Therefore, to optimize and ultimately maximize the science return from future polar as well as equatorial rover missions, we developed a traverse-planning algorithm, called *R-Traversal*. The algorithm uses regional data products from the Lunar Reconnaissance Orbiter (LRO) mission to identify least-energy traverse paths around key science and exploration targets while also considering the illumination conditions around the selected landing site and regions of resource interest.

* Corresponding author. Tel.: +1 480-965-6187.

E-mail address: espeyerer@asu.edu (E.J. Speyerer).

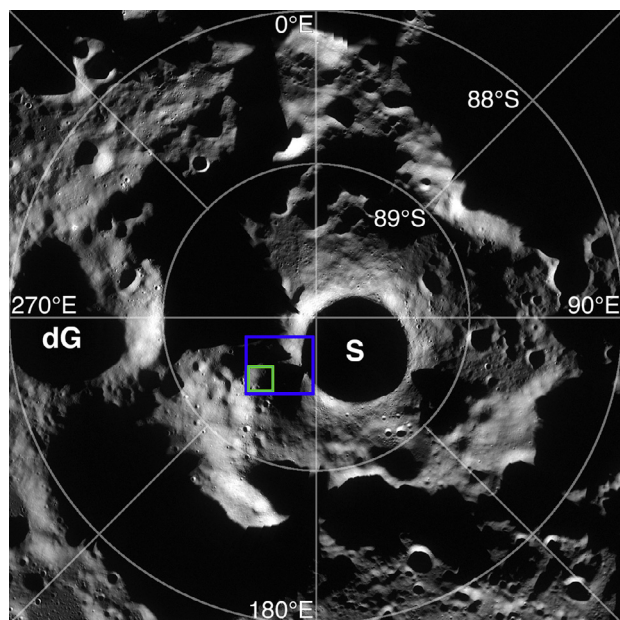


Fig. 1. LROC Wide Angle Camera context mosaic of the south pole with a blue box outlining our entire case study area and the smaller, green box outlining the area with stereo coverage. Shackleton and de Gerlache crater are marked with S and dG, respectively.

2. Resources for characterizing lunar exploration sites

The Lunar Reconnaissance Orbiter (LRO) mission and subsequently selected payload collect key observations to facilitate the planning of future surface missions. The orbital configuration enables observation of each polar region every 2 h, thus resulting in multi-temporal datasets that monitor variations over the year (i.e., visual and thermal observations) and strengthens datasets that accrue over thousands of successive orbits (i.e., altimeter and neutron measurements). For this study, we use data from the Lunar Reconnaissance Orbiter Camera (LROC), the Lunar Orbiter Laser Altimeter (LOLA), and the Diviner Lunar Radiometer Experiment collected near the south pole to analyze and construct optimal traverse paths for a potential polar rover on the rim of Shackleton crater and an adjacent ridge structure between Shackleton and de Gerlache crater (Fig. 1). The datasets and framework described in the following sections can be applied to many potential robotic and human exploration targets around the polar region as well as equatorial targets to optimize traverse paths and ensure scientific and/or exploration targets are accessible well before the launch of the mission.

2.1. Lunar Reconnaissance Orbiter camera (LROC)

LROC comprises a Wide Angle Camera (WAC) as well as twin Narrow Angle Cameras (NACs) with a nadir ground sampling distance of 75 m and 0.5 m from a 50 km orbit, respectively (Robinson et al., 2010). Since the start of the mission until 15 December 2015, the LROC team has acquired over 52,000 WAC and 114,000 NAC observations of the polar regions (poleward of $\pm 85^\circ$). These images enable mapping of the entire polar region as well as the identification of persistently illuminated regions (Speyerer and Robinson, 2013). The LROC team also acquired a subset of NAC images with increased exposure time (>11.8 ms; nominal polar exposures are 0.7 ms) for imaging inside regions that never receive direct sunlight, but only secondary illumination from nearby, sunlit crater rims (Koeber et al., 2014).

Additionally, over a series of orbits, the LROC NAC acquired a set of geometric stereo observations near the lunar poles. Unlike at equatorial sites, where the spacecraft is slewed in the cross-track direction to reimage the same area as the previous orbit (Henriksen et al., 2016), polar stereo observations require the spacecraft to pitch forward in one orbit, acquire an image, and reimage the same terrain in a nadir orientation during a subsequent orbit. Since the lighting is not always favorable near the poles (i.e., large areas in shadow), the LROC Science Operations Team commands an additional set of stereo observations when the solar azimuth shifts to illuminate areas previously in shadow in the original stereo pair. This process results in a set of stereo pairs collected at a pixel scale of 1.0 m due to cross-track pixel binning (pixel averaging) and increased integration time to boost the signal to noise in these images with grazing incidence angles (Robinson et al., 2010).

Each stereo pair in this study was processed using photogrammetric software developed by the German Aerospace Center (DLR) (Gwinner et al., 2009, 2010) to produce Digital Terrain Models (DTMs) sampled at 2.0 m/pixel (Fig. 2A). The individual DTMs were then mosaicked together to increase spatial coverage, which covered the illuminated portion of the connecting ridge between Shackleton and de Gerlache crater. The mosaicked NAC DTM has a mean absolute elevation offset of 0.62 m and a standard deviation of 1.20 m when compared to co-registered altimeter profiles discussed in the following section. While the resulting stereo derived DTMs provide precise knowledge of the illuminated terrain, the models lack topographic information inside areas shadowed during each set of stereo observations (i.e., such as persistently shaded craters) as well as areas along the rim of Shackleton crater.

2.2. Lunar Orbiter Laser Altimeter (LOLA)

The laser altimeter on LRO (LOLA) measures the distance between the instrument and the lunar surface with a range accuracy of 10 cm using a Q-switched Nd:YAG laser at 1064 nm and a set of avalanche photo diodes (Smith et al., 2010). The laser simultaneously illuminates five spots on the lunar surface, which are sensed by a set of detectors in the LOLA instrument. By measuring the time-of-flight, an accurate range measurement is derived for each laser spot. This configuration enables the LOLA instrument to collect measurements regardless of illumination conditions, including areas in permanent shadow. Using spacecraft ephemeris, these range measurements are reduced to elevation profiles. By combining the elevation profiles over many thousands of orbits, raster or gridded DTMs can be generated (Fig. 2B).

However, since the spacecraft ephemeris is not as accurate as the LOLA measurements, the gridded DTMs contain small vertical (up to 1 m) and horizontal (typically up to 6 m) offsets (Fig. 2B). Owing to the extensive number of orbit crossovers in the polar region, these relatively small offsets are visible in the final products and cause unrealistic values in derived slope maps. Recent work by Gläser and coworkers (2013) improved the precision and accuracy of these polar DTMs by combining the strengths of both LROC NAC stereo derived terrain models, which are very precise (horizontal accuracy = spatial resolution; Henriksen et al., 2016), and LOLA altimeter profiles, which are highly accurate (<10 m horizontally; Mazarico et al., 2013). After alignment, the LOLA tracks had a mean absolute elevation offset of 0.40 m and a standard deviation of 0.68 m when compared to the new regional DTM.

The resulting, adjusted DTM (Fig. 2C; Gläser et al., 2014) is both accurate and precise and thus makes it possible to sample elevation and compute accurate slopes on length scales relevant to a future polar prospector. The adjusted and refined DTM, which was sampled at 20 m/pixel, contains not only the portion of the connecting ridge covered by NAC stereo images, but also the entire

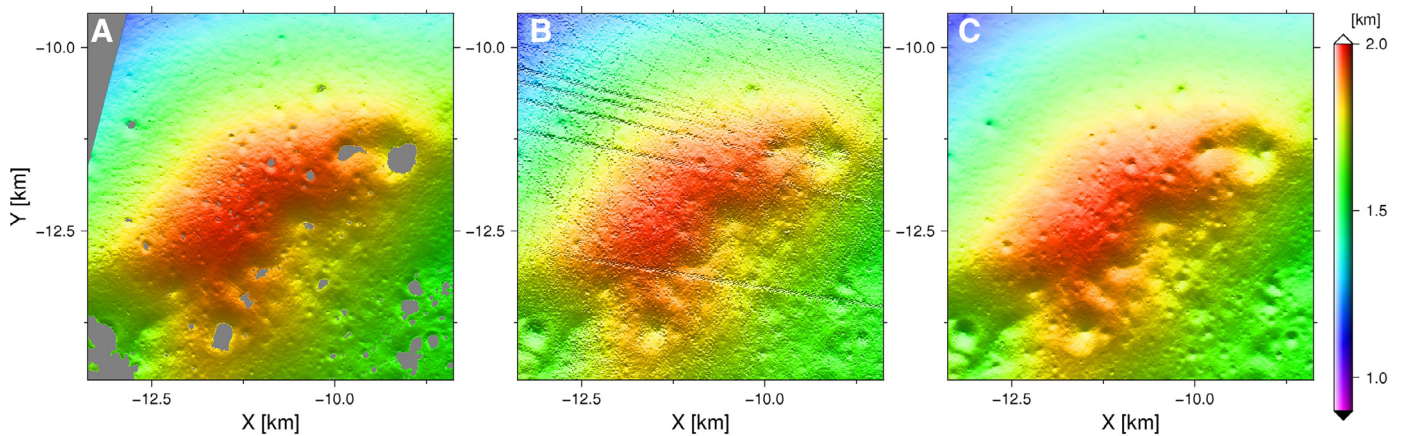


Fig. 2. Series of digital terrain models (DTMs) of the connecting ridge between Shackleton and de Gerlache crater derived using various techniques. This region is represented by the small, green box in Fig. 1. (A) 2 m/pixel LROC NAC derived DTM, gray areas indicate areas lacking topographic data due to being in shadow or outside the field of view. (B) LOLA DTM with visible errors due to offsets (up to 6 m lateral and 1 m vertical) in altimeter profiles. (C) Adjusted and refined DTM with no visible offset artifacts.

Table 1

Lunar soil trafficability parameters (Carrier et al., 1991).

Parameter	Value
Coefficient of soil/wheel cohesion, c_b	0.017 N/cm ²
Soil/wheel friction angle, ϕ_b	35°
Coefficient of soil slip, K	1.78 cm
Exponent of soil deformation, n	1 (dimensionless)
Cohesive modulus of soil deformation, k_c	0.14 N/cm ²
Frictional modulus of soil deformation, k_ϕ	0.82 N/cm ³

225 km² study area that includes both the connecting ridge and the highly-illuminated rim of Shackleton crater. The DTM enables accurate simulation of the illumination environment near the pole for any moment in time (Gläser et al., 2014). These lighting simulations offer the benefit of testing the illumination at a set distance above the lunar surface. For example, by testing the solar visibility 2 m above the surface, we are able to determine whether a solar panel positioned on top of a polar prospector could receive illumination at any given moment. Similar lighting simulations have been carried out on other elevation models derived using Earth-based radar and laser altimeter data with resolutions ranging from 474 to 20 m/pixels (Margot et al., 1999; Garrick-Bethell et al., 2005; Noda et al., 2008; Bryant, 2010; Bussey et al., 2010; Mazarico et al., 2011; De Rosa et al., 2012; McGovern et al., 2013; Gläser et al., 2014). Comparisons of these studies have shown that as the resolution and accuracy of the elevation model improves, more accurate lighting simulations can be derived as the true characteristics of the local topography are captured in the gridded DTM (see Fig. 23 and Table 1 in Gläser et al., 2014).

For this study, we use our adjusted and refined DTM sampled at 20 m/pixel (Gläser et al., 2014) to calculate local slopes encountered by the rover and to derive local illuminations conditions. While equatorial sites have the benefit of ~2.0 m/pixel NAC stereo DTMs, polar NAC DTMs over broad areas are not currently available and therefore, polar DTMs are limited by the density of LOLA spot measurements in the region. To date, the LOLA instrument has acquired over 1.1×10^7 measures between 89 and 90°S. However, producing a DTM at the finest spatial scale of 5 m, which is approximately the size of the laser spot on the lunar surface (Smith et al., 2010), results in a gridded DTM with 91% of the pixels being filled by interpolation. Therefore, we sampled the DTM at 20 m/pixel, which results in gridded DTM with only 22.7% of the points interpolated (Gläser et al., 2014). Alternatively, we could have created a merged DTM with 2 m/pixel resolution in areas

with NAC DTM coverage overlaid on 20 m/pixel LOLA topography. However, this would introduce resolution biases during the traverse planning. For example, a path through an area described by 2 m/pixel NAC topography might be avoided in favor of a neighboring area where the same small-scale topography is unknown and therefore relatively smooth, such as in an area modeled with the 20 m/pixel LOLA DTM.

Finally, it is possible to extrapolate the slopes derived by LOLA down to finer scales that will be encountered by a rover, assuming a self-affine surface. This relationship, which is commonly represented by the Hurst exponent (Hurst et al., 1965), varies depending upon the terrain being studied (Rosenburg et al., 2011). Therefore, we do not attempt to derive slopes at finer scales (e.g., length scale encountered by individual rover wheels or even down to the 2 m/pixel NAC DTM scale). As a result, for these first-order traverses that can be used for initial mission planning, we assume the slopes derived at the 20 m baseline are equivalent to the slopes encountered by each wheel. *R-Traverse* simulations can be executed with meter- and cm-scale topography to refine the optimal traverse plan around the exploration site if higher resolution data becomes available, or depending on the mission planning requirements. Nonetheless, these first-order optimal traverse paths enable mission planners to examine and strategize mission scenarios that account for general topography of the study region.

2.3. Diviner Lunar Radiometer Experiment

The Diviner Lunar Radiometer Experiment (DLRE; informally known as Diviner) measures infrared emission from the Moon using seven spectral channels spanning the wavelength range from 7.55 to 400 μ m (Paige et al., 2009). Using several of the bands, the Diviner team derived a series of model surface and subsurface temperature maps. Paige et al. (2010) used these thermal models to estimate the stability of ice at the surface and in the upper meter of the regolith. The resulting maps (see Fig. 1D in Paige et al., 2010) show areas near the poles where ice is stable at the surface and/or what depth is required to maintain stability (i.e., less than 1 kg/m²/Gyr loss). In the southern polar region, the maps indicate that surface and near-surface cold traps could harbor water over two thirds of the surface area poleward of 85°S and include areas in permanent shadow as well as areas that receive partial illumination throughout the year (Paige et al., 2010). These maps highlight key areas that future prospectors could target to test ice stability models as well as to assay potential volatile

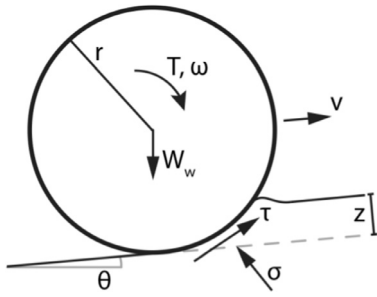


Fig. 3. wheel-soil interaction model where T =torque, ω =angular velocity, and v =wheel/rover velocity. All other parameters are defined in the text.

resources on the surface and at depth. In *R-Traversal*, we use the ice stability maps to identify key science targets and waypoints for a polar rover to investigate during the simulated missions (see S1 in the Supplementary Materials).

3. Modeling energy usage of a lunar rover

A model of the rover energy usage relies on surface properties of the regolith and the derived trafficability parameters that feed into estimates of wheel interaction over natural terrain. The Soil Mechanics Surface Sampler on Surveyor III and VIII as well as images collected documenting the interaction of the Surveyor spacecraft with the regolith provided the first estimates of the surface parameters (Scott, 1969; Costes et al., 1972). These estimates fed into the development of the Apollo Descent Stage, tools used by Apollo astronauts during extravehicular activities (EVAs), and vehicles such as the Modularized Equipment Transporter (MET) used during the Apollo 14 mission as well as the Lunar Roving Vehicle (LRV) that accompanied the Apollo 15, 16, and 17 missions.

After the Apollo missions, inspection of the spacecraft descent data, analysis of images and video documenting interactions with the regolith, vehicle data from the MET and LRV, penetration tests, as well as returned lunar samples helped researchers refine the trafficability parameters (reviewed by Mitchell et al., 1974). From the analysis of Apollo data as well as data from the Soviet Luna missions, Carrier and coauthors (1991, 2006) derived a common set of soil trafficability parameters for the Moon (Table 1).

While the trafficability parameters in Table 1 are directly traceable to measurements and observations obtained at surface exploration locations, none are necessarily representative of the regolith properties near the lunar poles. The areas in and around permanently shaded craters are extremely cold and volatile content in the regolith may drastically change the surface properties and subsequently the trafficability parameters in this temperature regime. For this study, however, we used the trafficability parameters described in Table 1.

The mechanics and interaction of a rigid wheel over natural, deformable terrain are well known (Bekker, 1956; Bekker, 1960; Bekker, 1964; Janosi and Hanamoto, 1961; Wong, 1989; Shibly et al., 2005; Ishigami et al., 2007). In these cases, the force from the mass of the wheel and vehicle cause the rigid wheel (i.e., not pneumatic) to sink into the softer, deformable soil. Bekker introduced one popular model in the 1950's and 1960's, which focused on calculating the normal, σ , and tangential, τ , stresses acting upon the wheel-soil interface (Fig. 3). From this foundation, Bekker derived a series of relationships that modeled the effect of a wheeled vehicle traveling over a deformable terrain. This work included motion resistances due to regolith compaction, which is a direct result of the wheel load causing the wheel to compress the

soil and form a rut with a depth, z :

$$z = \left(\frac{3W_w}{b(3-n)\left(\frac{k_c}{b} + k_\phi\right)\sqrt{2r}} \right)^{\left(\frac{2}{2n+1}\right)} \quad (1)$$

where W_w is the vertical load applied by the wheel, b is the wheel width, and r is the wheel radius. The resulting compaction of the regolith, introduces the following resistance to motion:

$$R_c = b \left[\left(\frac{k_c}{b} + k_\phi \right) \frac{z^{n+1}}{n+1} \right] \quad (2)$$

In addition, a bulldozing resistance can apply a force against the wheel when the weighed wheel displaces a significant amount of regolith. This resistance is defined as:

$$R_b = \frac{b \sin(\alpha + \phi)}{2 \sin(\alpha) \cos(\phi)} [2z c_b K_c + \rho g z K_\gamma] + \frac{\pi t^2 \rho g \left(\frac{\pi}{2} - \phi\right)}{3} + \frac{\pi c_b t}{180} + c_b l^2 \tan\left(\frac{\pi}{4} - \frac{\phi}{2}\right) \quad (3)$$

where α , K_c , K_γ , and l are angle of approach, the modulus of density of soil deformation, modulus of cohesion of soil deformation, and soil disruption depth, respectively, and are defined as:

$$\alpha = \cos^{-1} \left(1 - \frac{z}{r} \right) \quad (4)$$

$$K_c = [N_c - \tan(\phi)] \cos^2(\phi) \quad (5)$$

$$K_\gamma = \left[\frac{2N_\gamma}{\tan(\phi)} + 1 \right] \cos^2(\phi) \quad (6)$$

$$l = z \tan^2 \left(\frac{\pi}{4} - \frac{\phi}{2} \right) \quad (7)$$

where N_c and N_γ are non-dimensional coefficients that are functions of the soil/wheel friction angle. For the lunar case where the soil/wheel friction angle is 35° , N_c and N_γ are 57.8 and 47.3, respectively (Terzaghi, 1943).

The final longitudinal force considered for a rover on deformable terrain is the force encountered during a change in elevation:

$$R_g = W_v \sin(\theta) \quad (8)$$

where W_v is the weight of the vehicle and θ is the local slope (R_g is negative in cases where the slope is decreasing). The resistance forces defined in Eqs. (2), (3) and (8) combine to determine the total tractive effort for the entire rover where n is the number of wheels included in the rover design:

$$TTE = n(R_c + R_b) \pm R_g \quad (9)$$

This effort can then be used to calculate the required energy, E (Joules), required for the rover to move across the deformable terrain at a constant velocity and a set distance, d :

$$E = |(TTE \times d)| \quad (10)$$

Using this model and the pre-defined trafficability parameters (Table 1), we estimate the energy required to move a four-wheeled rover over lunar regolith with homogeneous properties (Fig. 4). For this study, we assume a rover mass of 700 kg with non-porous wheels that evenly distribute the vertical load. The mass is comparable to the Apollo LRV that transported astronauts, samples, and experiments. Like the LRV, each wheel used in our model has a diameter of 81.8 cm and a width of 22.9 cm (Asnani et al., 2009). As seen in Fig. 4, the energy required to rove across the modeled terrain at a constant speed (expressed in N-m) changes as a function

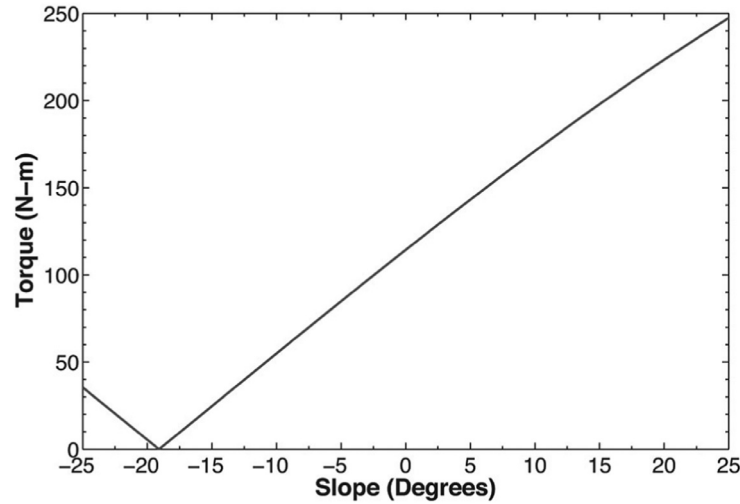


Fig. 4. Torque required for the modeled rover to traverse over varying slopes (note: torque must be applied in the opposite direction to sustain a constant speed when the slope steeper than -19° from horizontal).

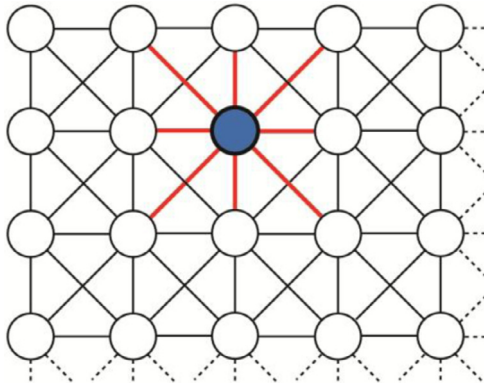


Fig. 5. Example of the gridded mesh structure. The blue node represents the current node and the red edges indicate ones currently tested during this iteration. Each edge has a different value assigned to it based on the local slope encounter between the current and neighboring node.

of local slope. By varying the rover parameters, such as the mass and number and size of the wheels, the energy requirement and effectiveness of a rover/wheel design in a given environment can be assessed.

4. Path planning and optimization

To locate potential traverse options around the polar region, and ultimately the least-energy traverse path, we define a 2-D gridded mesh and overlay it on the DTM. This gridded mesh creates a set of evenly spaced nodes that match the grid spacing of the input DTM (Fig. 5). Each of the nodes is connected to up to eight neighboring nodes, and each connection, or edge, is assigned a value that corresponds to the amount of energy required for a rover to move from the current node to the corresponding neighboring node. These energy requirements are derived using the local slope derived from the DTM and the terramechanics model described in the previous section. We assume that the elevations represented in the DTM accurately characterize the true topography, therefore we can only estimate the optimal path since the true elevation changes may differ from the DTM due to vertical errors as well as small scale topographic changes and obstacles not captured at the scale of the DTM.

To estimate the energy required over the entire traverse, the sum of the edges along the traverse are calculated. To find the least-energy traverse path, we minimize the sum of the edges along the traverse. Numerous optimization techniques developed over the years have solved these types of gridded mesh (or graph) search problems, commonly referred to as shortest-path problems. Dijkstra's graph search algorithm is commonly used to find the least-cost, or in our case the least-energy traverse path from one node in the mesh to every other node (Dijkstra, 1959). In large, dense meshes such as the ones employed here, Dijkstra's algorithm is inefficient. However, Hart and associates (1968) improved the performance of Dijkstra's algorithm by incorporating a heuristic component to converge on the optimal solution faster by deterring the exploration of nodes in the "wrong direction" of a goal or target node. This extension to the Dijkstra's algorithm is commonly called A* (pronounced A-star). The heuristic function estimates the energy required to move from an intermediate node to the target node:

$$f(n) = g(n) + h(n) \quad (11)$$

where $g(n)$ is the total cost, or in this case energy, to reach the current node from the starting node; $h(n)$ is the heuristic or estimated energy to reach the target node from the current node; and $f(n)$ is the estimated total cost required to travel from the starting node to the target node. If the heuristic, $h(n)$, is chosen well, the efficiency of the graph search algorithm drastically improves making it possible to identify long, optimal traverses with few deviations during the search.

To use the A* algorithm in our study, we first create a lower resolution heuristic matrix and later use the results when computing the final optimal traverse(s) on the full resolution DTM. The heuristic matrix estimates the total energy required to travel from any node in the mesh to any other node in the mesh and is computed once for each DTM (Fig. 6A). For large mesh structures, such as the ones used in this study, it is impractical to calculate $h(n)$ for each node in the original, full-resolution mesh. Therefore, to create the heuristic matrix, we first reduce the resolution of our gridded mesh over the DTM. By doing so, we drastically reduce the number of nodes and corresponding edges in the mesh. We empirically derived the level of reduction to balance the time and storage space required for pre-computing the heuristic and the accuracy of heuristic. Once reduced, we use the Floyd-Warshall algorithm (Floyd, 1962; Warshall, 1962) and our terramechanics model described in the previous section to find the least-energy traverses

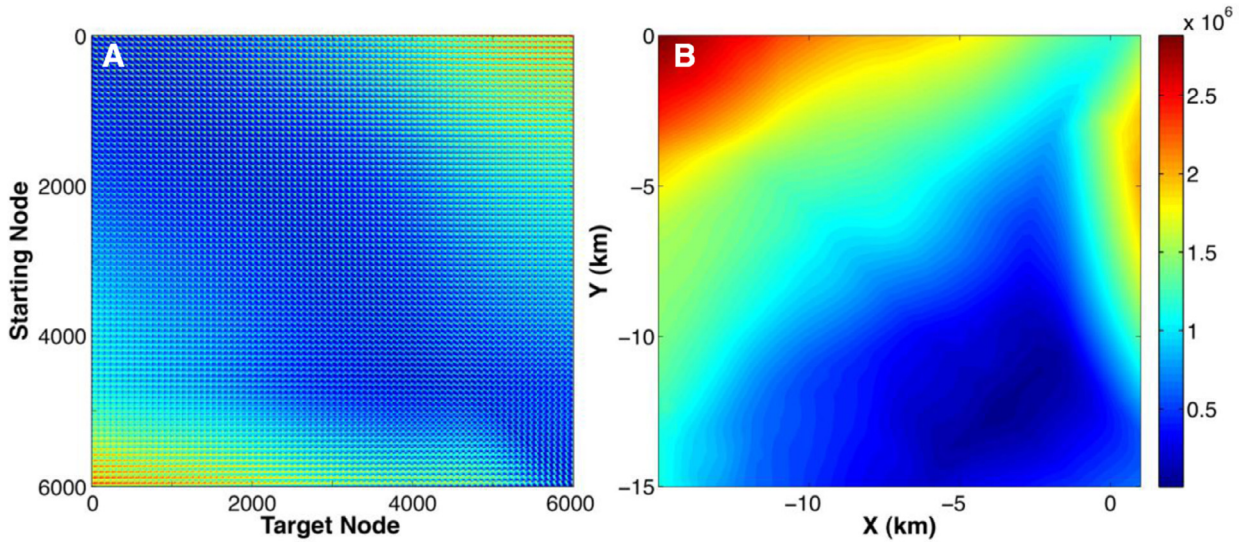


Fig. 6. Example of a heuristic matrix and map. (A) The heuristic matrix quantifies the energy required for the rover to traverse any node in the reduced mesh to any other node in the reduced mesh. (B) The heuristic map quantifies the energy required by the modeled rover to traverse from any point on the map to the target node (PSR-1; see Table 2). In this example, the heuristic matrix is calculated with a node spacing of 200 m for speed and storage considerations and resampled with a bilinear interpolation to 20 m when used in the A* algorithm.

from each node in the reduced mesh to every other node in the mesh. The Floyd–Warshall algorithm examines every path combination to identify the amount of energy or torque required to traverse from one node to any other node in the mesh structure. The heuristic matrix is $n \times n$ with n being the number of nodes in the reduced mesh structure (Fig. 6A). Using this matrix, we then create heuristic maps for each waypoint, by selecting the column in the heuristic matrix that corresponds to the target node and reshaping it back into the original reduced gridded form (Fig. 6B). We then enlarge the heuristic map to match the original mesh using a bilinear interpolation and use it as the A* heuristic component to efficiently identify least-energy traverses using the 20 m LROC-NAC/LOLA DTM.

The speed of the A* search algorithm depends on the quality and magnitude of the heuristic. A heuristic that underestimates the required energy to traverse to the destination will take longer to find the optimal traverse, but will assure that the optimal traverse will be identified. In the opposite case, where the heuristic overestimates the required energy to traverse to the destination, the A* search algorithm could overlook the optimal solution due to an overestimation in $f(n)$. In the extreme case, the A* search algorithm would act more like a greedy best-first search or pure heuristic search algorithm and only rely on the heuristic to find a path. In *R-Traversal*, we can scale the heuristic component in Eq. (11) to speed up or increase the quality of the traverse. However, for the following case studies, we have selected not to scale the heuristic values to ensure we identify the optimal traverse.

In our simulation, the initial scaling applied to compute the heuristic does not alter the final optimal traverse identified, but only impacts the time required to locate the optimal traverse path. For example, if the DTM was not scaled when computing the heuristic matrix, the optimal traverse path could be identified without any deviation, since in this case the heuristic would be equivalent to the true cost function of the remaining traverse. However, in cases where the DTMs are large, the time and computational requirements to compute the heuristic are not practical. Therefore, we reduce the number of nodes in our mesh structure and later rescale it back to the original resolution (20 m in this case) and identify optimal traverses. This rescaling removes small-scale topography that the rover would encounter and traverse around. Therefore, when scaled back to the original resolu-

tion, the heuristic will underestimate and at best match the true energy requirements derived from the full resolution DTM. This ensures, as previously stated, that *R-Traversal* will find the optimal traverse path.

To incorporate time-varying components, such as solar illumination, the 2-D gridded mesh is replaced with a 3-D mesh. The first two dimensions of the mesh denote the lateral position of the rover while the third records the temporal component. In this configuration, there are nine paths or edges to which the rover can traverse to: the eight neighboring nodes (Fig. 5) or the current node. By selecting the current node, the rover does not move during the sampled time step. For this technique, we use the heuristic component derived from the static case and the same A* algorithm to locate the paths and associated timing of the traverse. By incorporating time-varying components into the traverse optimization, we can ensure the areas are accessible and ample solar energy will be available for the rover throughout the traverse.

Planning an entire mission and not just a traverse from point A to point B, a user pre-selects the full area of interest and the amount of time spent at each site, thus allowing for detailed sampling and measurements requiring extended integration times. These areas of interest are then fed into the *R-Traversal* as waypoints. The algorithm then takes the initial starting location (i.e., landing site) and the list of waypoints and derives optimal traverses between each. The initial heuristic matrix also aids in ordering the waypoints to identify the optimal ordering of the waypoints in the simulated traverse.

5. Exploration planning using static datasets

The datasets and framework described above identify optimal traverses around many different exploration and scientific targets. In this section, we will examine one possible traverse along the rim and near Shackleton crater, which is a 21 km diameter impact crater near the south pole (89.655°S, 129.2°E) with 235 km² of its interior in perpetual shadow (Nozette et al., 1996; Bussey et al., 1999; Zuber et al., 2012; Speyerer and Robinson, 2013). The first images of the region provided by the Clementine UVVIS camera indicated that a portion of the rim was persistently illuminated (Nozette et al., 1996; Bussey et al., 1999). With images and topographic data returned by LRO, knowledge of these regions of

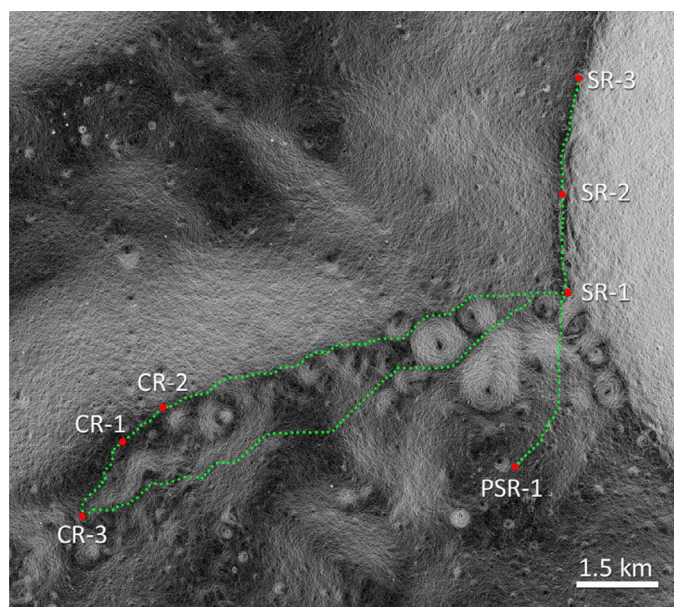


Fig. 7. Map of optimal traverses between neighboring stations overlaid on a NAC/LOLA slope map.

persistent illumination were refined and quantified (Mazarico et al., 2011; Speyerer and Robinson, 2013).

Nearly-persistent illumination is desired for a long-duration mission to survive without the benefit of a Radioisotope Thermoelectric Generator near the lunar poles. One approach to achieve this, is to land in a persistently illuminated region where eclipse periods are short (<150 h). An alternative would be to have a rover follow the sunlight and extend the amount of illumination received. Speyerer and Robinson (2013) identified several areas where nearly continuous illumination can be achieved over the course of an entire year with just a modest amount of surface mobility.

Using the 20 m/pixel LROC NAC/LOLA-derived DTM of the south polar region (Gläser et al., 2014) and *R-Traversal*, we identified the optimal path between a set of three highly illuminated points (SR-1, SR-2, and SR-3) along the rim of Shackleton crater (Fig. 7; Tables 2 and 3). Multi-temporal WAC images showed that the three points, or stations, were collectively illuminated for 94% of the lunar year (Speyerer and Robinson, 2013). By configuring a network of solar panels and/or traversing between the three stations, the total period of time illuminated can be significantly extended. Since the energy required traversing uphill differs from downhill the optimal (least-energy) traverses in one direction differ slightly from the optimal traverses in the opposite direction. In all, the mean absolute slope (at a 20 m baseline) among all the traverses between stations on the rim of Shackleton is 2.9° with a maximum uphill slope of 10.8° . These slopes are well within the range of previous rover designs and many proposed rovers designs.

The rim of Shackleton crater, like many other lunar craters, is very narrow (~ 10 s– 100 m across) making it difficult to land a rover near the three Shackleton rim sites. However, a connecting ridge (CR) located off the rim of the Shackleton crater along the 205°E meridian toward de Gerlache crater offers an ideal place to land a small spacecraft and launch a rover. One area along the ridge in particular, (CR-1), was a candidate landing site for the European Space Agency's Lunar Lander project (Fisackerly et al., 2011). De Rosa and coauthors (2012) showed that the connecting ridge between Shackleton and de Gerlache crater has relatively benign slopes (mean slope $<5^\circ$ at a 5 m baseline; standard deviation of slope 3.2°), sparse population of boulders (20 km^{-2}),

and long periods of continuous illumination. Speyerer and Robinson (2013) identified two other stations (designated CR-2 and CR-3 in this study; Fig. 7; Table 2 and 3) near the CR-1 landing site, which collectively remain illuminated for 91.8% of the year and were eclipsed for only 104 h during the lunar year sampled. The two stations are separated by only 2.62 km with a mean absolute slope of 2.6° . An 8.36 km traverse from station CR-2 with a mean slope of 5.9° and max uphill slope of 9.7° leads to Station SR-1 on the rim of Shackleton crater.

By incorporating model-calculated ice stability maps generated from Diviner radiometer data (S1 in Supplementary Materials), we can identify locations where ice is stable at the surface or at shallow depths (<1 m). Although the floor of Shackleton crater contains a vast area where ice is stable at the surface (Paige et al., 2009; Zuber et al., 2012), the steep crater walls and permanent shadow complicate traverses and long-duration operations. However, the rim of the crater houses small pockets where ice is stable at shallow depths (0.4–1.0 m) (Paige et al., 2010). These localized cold regions are not only easily accessible while the rover is traversing between persistently illuminated stations; the terrain is also illuminated for at least part of the year. Moreover, there are also several locations near the rim of Shackleton where thermal models indicate that ice is stable at the surface (S1 in the Supplementary Materials). Like the floor of Shackleton crater, both of these topographic depressions are in permanent shadow. One of the permanently shadowed regions (PSR-1: 89.575°S , 196.8°E) examined has a maximum surface temperature of 78.9 K, which is comparable to the temperatures inside Shackleton crater (near 75 K). However, unlike Shackleton crater, a small boom that elevates the solar panel a few meters off the surface can access solar energy for the rover while in this extreme environment. The slopes encountered during a traverse into and out of the depression are also gentler ($<10^\circ$) in comparison with entering a larger PSR such as Shackleton ($\sim 32^\circ$).

6. Exploration planning using dynamic datasets

The extreme lighting environment near the lunar poles not only creates a broad disparity between persistently illuminated regions and regions in permanent shadow, but also imposes abrupt changes to the illumination conditions as the Sun is eclipsed by nearby and distant topographic highs. To maintain long-duration solar powered operations near the pole, lighting simulations using LROC-NAC/LOLA topography forecast eclipse periods (Gläser et al., 2014) and *R-Traversal* integrates this information to avoid long periods in shadow. For this study, we examined traverses in the vicinity of Shackleton crater and identified time-dependent traverses to keep the rover illuminated using 20 m/pix lighting simulations over a one-year period starting on 1 January 2021 and concluding on 31 December 2021.

In this case study, the traverse started at the CR-1 landing site (De Rosa et al., 2012) and allowed the rover to travel along the connecting ridge toward Shackleton crater. In the simulation, the rover was allowed to move only when the solar panels received direct illumination and remained stationary for periods when the Sun was eclipsed. We assumed that the direct sunlight received was sufficient to move the rover without stopping to charge the battery. We found that with a maximum speed of 30 m/h (0.83 cm/s), the rover remained illuminated for 94.43% of the year with the longest eclipse lasting 101 h. During this year-long period, the rover moved a total of 22.11 km at an average speed of 2.5 m/h and never left the connecting ridge with the complete traverse staying close to the three CR sites (Fig. 7; Table 2; S2 in the Supplementary Materials). Increasing the maximum speed to 60 m/h (1.6 cm/s), boosted the total time illuminated by only 0.02% and added 665 m to the total traverse distance due to a

Table 2

Station locations and illumination statistics collected over a 1-year period (1 January 2021 to 31 December 2021) using 1-h time intervals. For each location, we calculate the average Sun visibility (mean of the Boolean Sun visible/not visible) and the average Sun illumination (mean of the normalized solar disc area visible).

Station	Location		Average Sun visibility	Average Sun visibility	Average Sun illumination	Longest eclipse period 2 m
	Latitude, °	Longitude, °E	at the surface, %	2 m above the surface, %	2 m above the surface, %	above surface, h
SR-1	−89.685	196.7	49.25	86.71	82.71	135
SR-2	−89.740	201.2	42.64	79.35	75.04	359
SR-3	−89.808	205.9	43.40	55.50	51.02	1144
CR-1	−89.468	222.6	20.15	46.56	40.67	1421
CR-2	−89.500	222.1	44.44	49.87	46.31	1188
CR-3	−89.418	221.3	50.01	60.41	58.82	891
PSR-1	−89.575	196.7	0	0	0	n/a

Table 3

Optimal traverse statistics based on least-energy usage between the various south pole stations defined in Table 2. The table provides the distance needed to travel (km) and the mean absolute slope (°) along the optimal traverse.

Distance (km)/mean(abs(slope))		Ending node						
		SR-1	SR-2	SR-3	CR-1	CR-2	CR-3	PSR-1
Starting node	SR-1	–	1.85/2.9	4.02/3.3	9.36/5.5	8.36/5.8	10.67/5.0	3.63/8.7
	SR-2	1.85/2.9	–	2.25/2.2	10.01/4.9	9.01/5.1	11.31/4.3	5.39/6.6
	SR-3	4.02/3.2	2.25/2.2	–	11.26/7.0	10.26/7.4	12.57/6.7	7.65/5.3
	CR-1	9.36/5.6	10.01/5.7	12.27/5.0	–	1.00/2.8	1.69/2.3	7.47/6.7
	CR-2	8.36/5.9	9.02/6.0	11.27/5.2	1.00/2.9	–	2.62/2.7	6.98/6.8
	CR-3	10.67/5.0	11.33/5.1	13.58/4.6	1.69/2.3	2.62/2.6	–	8.39/5.6
	PSR-1	3.64/8.2	5.40/6.3	7.65/5.1	7.47/6.7	6.98/6.7	8.40/5.7	–

quick traverse to a nearby illuminated peak while the original traverse area was eclipsed (S3 in the Supplementary Materials). Each of these scenarios provides opportunities for long-duration stops along the traverse for the prospector to drill, measure, and sample nearby terrain. (Simulations of the traverses are available in the online supplementary materials: S2 and S3). Custom stops at key science targets as well as stops to charge (if required by the rover architecture) can be integrated into the path planning routine, if necessary. However, in these simulations where we are maximizing the solar energy captured by the rover's solar panel, we omitted these periotic stops.

7. Conclusions

To fully understand the extent and chemistry of the cold-trapped volatiles both spatially and laterally, ground-truth measurements that sample the form, local distribution, and concentration are required across a broad range of targets. These types of measurements are ideal for comparing to orbital neutron spectrometer measurements, which indicate the presence of H in the upper meter of regolith. Determining optimal traverses based on data from the LROC, LOLA, and Diviner provides a solid foundation for mission concept planning. The grazing incidence angles near the lunar poles create many pockets of permanent and persistent shadow in this region; a long-duration rover with a suitably instrumented payload could evaluate volatiles (type and grade) in multiple small, shadow-induced cold traps and examine how the quantity and composition of volatiles change in areas that receive different percentages of sunlight. These varied investigations would also address questions about the mobility of volatiles over short time scales as a region falls in and out of shadow. In addition, SR-1, SR-2, and SR-3 offer ideal views inside of a large PSR (floor of Shackleton crater). From these locations, standoff instruments could assess surface deposits without risking a traverse down the steep walls.

The present study represents a first step in assessing trafficability in the polar regions. The terramechanics model described is

flexible and can be used to examine multiple rover and wheel configurations. In addition, *R-Traverse* can also be adapted for other planetary bodies by altering the trafficability parameters. In the case for the lunar poles, future iterations of the model could be improved by considering surface property measurements derived from laboratory experiments with varying amounts of water ice mixed with lunar regolith simulants such as JSC-1A (mare) and NU-LHT-2M (highland) under appropriate thermal conditions. Results from these experiments may provide additional approximations and constraints for trafficability parameters for regolith encountered near the lunar poles.

R-Traverse provides the means to evaluate trafficability and determine optimal traverses using high-resolution DTMs. From this foundation, realistic traverses around potential landing sites and select science targets are possible. Finally, with the introduction of dynamic datasets (e.g., changing solar illumination over time) we can identify the precise timing and sequencing of science stops or waypoints. As a proof-of-concept we determined an optimal traverse between highly illuminated peaks near Shackleton crater stopping to investigate small permanently shaded craters where ice may be stable at the surface at geologic timescales. In addition, we investigated a time-dependent traverse that maximizes the solar energy captured by a rover over a period of one year, enabling future feasibility studies.

Acknowledgment

The authors would like to acknowledge support for this work from the Lunar Advanced Science and Exploration Research (LASER) program under NASA grant [NNX13AJ68G](#) (PI: S. Lawrence) and the dedication of the LRO Science Teams that produced an invaluable dataset to plan and assist future human and robotic exploration of the Moon.

Supplementary materials

Supplementary material associated with this article can be found, in the online version, at [doi:10.1016/j.icarus.2016.03.011](#).

References

- Andrews, D.R., Colaprete, A., Quinn, J., et al., 2014. Introducing the resource prospector (RP) mission. In: AIAA SPACE 2014 Conference and Exposition, SPACE Conferences & Exposition. American Institute of Aeronautics and Astronautics. doi:10.2514/6.2014-4378.
- Asnani, V., Delap, D., Creager, C., 2009. The development of wheels for the Lunar roving vehicle. *J. Terramech.* 46, 89–103. doi:10.1016/j.jterra.2009.02.005.
- Bekker, M.G., 1956. *Theory of Land Locomotion the Mechanics of Vehicle Mobility*. University of Michigan Press, Ann Arbor, MI, USA.
- Bekker, M.G., 1960. *Off-The-Road Locomotion*. The University of Michigan Press, Ann Arbor, MI, USA.
- Bekker, M.G., 1964. Mechanics of locomotion and lunar surface vehicle concepts. SAE Technical Paper 640049. doi: 10.4271/640049.
- Bryant, S., 2010. Lunar pole illumination and communications statistics computed from GSSR elevation data. In: SpaceOps 2010 Conference. Huntsville, Alabama pp. AIAA-2010-1913.
- Bussey, D.B.J., McGovern, J.A., Spudis, P.D., et al., 2010. Illumination conditions of the south pole of the Moon derived using Kaguya topography. *Icarus* 208, 558–564. doi:10.1016/j.icarus.2010.03.028.
- Bussey, D.B.J., Spudis, P.D., Robinson, M.S., 1999. Illumination conditions at the lunar South Pole. *Geophys. Res. Lett.* 26, 1187–1190. doi:10.1029/1999GL900213.
- Carrier, D.W., 2006. Lunar soil simulation and trafficability parameters. Lunar Geological Institute (http://www.lpi.usra.edu/lunar/surface/carrier_lunar_trafficability_param.pdf).
- Carrier, W.D., Olhoeft, G.R., Mendell, W., 1991. Physical properties of the lunar surface. In: Heiken, G., Vaniman, D., French, B.M. (Eds.), *Lunar Sourcebook*. Cambridge University Press, Cambridge, pp. 475–594.
- Colaprete, A., Schultz, P., Heldmann, J., et al., 2010. Detection of water in the LCROSS ejecta plume. *Science* 330, 463–468. doi:10.1126/science.1186986.
- Costes, N.C., Farmer, J.E., George, E.B., 1972. *Mobility Performance of the Lunar Roving Vehicle: Terrestrial Studies – Apollo 15 Results*. Washington, D.C.
- De Rosa, D., Bussey, B., Cahill, J.T., et al., 2012. Characterisation of potential landing sites for the European Space Agency's Lunar Lander project. *Planet. Space Sci.* 74, 224–246. doi:10.1016/j.pss.2012.08.002.
- Dijkstra, E.W., 1959. A note on two problems in connexion with graphs. *Numer. Math.* 1, 269–271.
- Feldman, W.C., 1998. Fluxes of fast and epithermal neutrons from lunar prospector: Evidence for water ice at the lunar poles. *Science* 281, 1496–1500. doi:10.1126/science.281.5382.1496.
- Feldman, W.C., Lawrence, D.J., Elphic, R.C., et al., 2000. Polar hydrogen deposits on the Moon. *J. Geophys. Res.* 105, 4175–4195. doi:10.1029/1999JE001129.
- Fisackerly, R., Pradier, A., Gardini, B., et al., 2011. The ESA Lunar Lander Mission. In: AIAA SPACE 2011 Conference & Exposition, SPACE Conferences & Exposition. American Institute of Aeronautics and Astronautics, p. 7217. doi:10.2514/6.2011-7217.
- Floyd, R.W., 1962. Algorithm 97: Shortest path. *Commun. ACM* 5, 345. doi:10.1145/367766.368168.
- Garrick-Bethell, I., Byrne, S., Hoffman, J.A., et al., 2005. Areas of favorable illumination at the lunar poles calculated from topography, in: *Lunar Planet. Sci. XXXVI*. Houston, TX, p. #2006.
- Gläser, P., Haase, I., Oberst, J., et al., 2013. Co-registration of laser altimeter tracks with digital terrain models and applications in planetary science. *Planet. Space Sci.* 89, 111–117. doi:10.1016/j.pss.2013.09.012.
- Gläser, P., Scholten, F., De Rosa, D., et al., 2014. Illumination conditions at the lunar south pole using high resolution Digital Terrain Models from LOLA. *Icarus* 243, 78–90. doi:10.1016/j.icarus.2014.08.013.
- Gwinner, K., Scholten, F., Preusker, F., et al., 2010. Topography of Mars from global mapping by HRSC high-resolution digital terrain models and orthoimages: Characteristics and performance. *Earth Planet. Sci. Lett.* 294, 506–519. doi:10.1016/j.epsl.2009.11.007.
- Gwinner, K., Scholten, F., Spiegel, M., et al., 2009. Derivation and validation of high-resolution digital terrain models from Mars express HRSC data. *Photogramm. Eng. Remote Sens.* 75, 1127–1142. doi:10.14358/PERS.75.9.1127.
- Hart, P., Nilsson, N., Raphael, B., 1968. A formal basis for the heuristic determination of minimum cost paths. *IEEE Trans. Syst. Sci. Cybernet.* 4, 100–107. doi:10.1109/TSSC.1968.300136.
- Henriksen, M.R., Manheim, M.R., Burns, K.N., et al., 2016. Extracting accurate and precise topography from LROC narrow angle camera stereo observations. *Icarus*.
- Hurley, D.M., Gladstone, G.R., Stern, S.A., et al., 2012. Modeling of the vapor release from the LCROSS impact: 2. Observations from LAMP. *J. Geophys. Res. Planets* 117, E00H07. doi:10.1029/2011JE003841.
- Hurst, H., Black, R., Simaika, Y., 1965. *Long-Term Storage: An Experimental Study*. Constable, London.
- Ishigami, G., Miwa, A., Nagatani, K., et al., 2007. Terramechanics-based model for steering maneuver of planetary exploration rovers on loose soil. *J. F. Robot.* 24, 233–250. doi:10.1002/rob.20187.
- Janosi, Z., Hanamoto, B., 1961. *An Analysis of the Drawbar Pull vs Slip Relationship for Track Laying Vehicles*. Land Locomotion Laboratory.
- Koeber, S.D., Robinson, M.S., Speyerer, E.J., 2014. LROC Observations of permanently shadowed regions on the Moon. In: 45th Lunar and Planetary Science Conference.
- Mazarico, E., Neumann, G.A., Smith, D.E., et al., 2011. Illumination conditions of the lunar polar regions using LOLA topography. *Icarus* 211, 1066–1081. doi:10.1016/j.icarus.2010.10.030.
- Mazarico, E., Goossens, S.J., Lemoine, F.G., et al., 2013. Improved orbit determination of lunar orbiters with lunar and gravity fields obtained by the GRAIL mission. In: 44th Lunar and Planetary Science Conference.
- McGovern, J.A., Bussey, D.B., Greenhagen, B.T., et al., 2013. Mapping and characterization of non-polar permanent shadows on the lunar surface. *Icarus* 223, 566–581. doi:10.1016/j.icarus.2012.10.018.
- Mitchell, J.K., Houston, W.N., Carrier, W.D., et al., 1974. Apollo soil mechanics experiment S-200. Final report, NASA Contract NAS 9-11266, Space Sciences Laboratory Series 14, Issue 7, Univ. of California, Berkeley.
- Mitrofanov, I.G., Sanin, A.B., Boynton, W. V., et al., 2010. Hydrogen mapping of the lunar south pole using the LRO neutron detector experiment LEND. *Science* 330, 483–486. doi:10.1126/science.1185696.
- Noda, H., Araki, H., Goossens, S., et al., 2008. Illumination conditions at the lunar polar regions by KAGUYA (SELENE) laser altimeter. *Geophys. Res. Lett.* 35, L24203. doi:10.1029/2008GL035692.
- Nozette, S., Lichtenberg, C.L., Spudis, P., et al., 1996. The Clementine bistatic radar experiment. *Science* (80.), 274, 1495–1498. doi:10.1126/science.274.5292.1495.
- Paige, D.A., Foote, M.C., Greenhagen, B.T., et al., 2009. The Lunar Reconnaissance Orbiter Diviner Lunar Radiometer Experiment. *Space Sci. Rev.* 150, 125–160. doi:10.1007/s11214-009-9529-2.
- Paige, D.A., Siegler, M.A., Zhang, J.A., et al., 2010. Diviner lunar radiometer observations of cold traps in the Moon's South Polar Region. *Science* 330, 479–482. doi:10.1126/science.1187726.
- Robinson, M.S., Brylow, S.M., Tschimmel, M., et al., 2010. Lunar Reconnaissance Orbiter camera (LROC) instrument overview. *Space Sci. Rev.* 150, 81–124. doi:10.1007/s11214-010-9634-2.
- Rosenburg, M.A., Aharonson, O., Head, J.W., et al., 2011. Global surface slopes and roughness of the Moon from the lunar orbiter laser altimeter. *J. Geophys. Res.* 116, E02001. doi:10.1029/2010JE003716.
- Scott, R.F., Roberson, F.I., 1969. Soil mechanics surface sampler, in: *Surveyor: Program Results*. Washington, D.C., pp. 171–180.
- Shibly, H., Iagnemma, K., Dubowsky, S., 2005. An equivalent soil mechanics formulation for rigid wheels in deformable terrain, with application to planetary exploration rovers. *J. Terramechanics* 42, 1–13. doi:10.1016/j.jterra.2004.05.002.
- Smith, D.E., Zuber, M.T., Neumann, G.A., et al., 2010. Initial observations from the lunar orbiter laser altimeter (LOLA). *Geophys. Res. Lett.* 37, L18204. doi:10.1029/2010GL043751.
- Speyerer, E.J., Robinson, M.S., 2013. Persistently illuminated regions at the lunar poles: Ideal sites for future exploration. *Icarus* 222, 122–136. doi:10.1016/j.icarus.2012.10.010.
- Spudis, P.D., 2011. The moon: Port of entry to cislunar space. In: Lutes, C.D., Hays, P.L. (Eds.), *Toward a Theory of Space Power: Selected Essays*. National Defense University Press, Washington, D.C., pp. 241–251.
- Spudis, P.D., Lavoie, T., 2010. Mission and implementation of an affordable lunar return. In: *Space Manufacturing 14 Conference*. Space Studies Institute, p. 30.
- Terzaghi, K., 1943. *Theoretical Soil Mechanics*. J. Wiley and Sons, inc..
- Warshall, S., 1962. A theorem on Boolean matrices. *J. ACM* 9, 11–12. doi:10.1145/321105.321107.
- Wong, J., 1989. *Terramechanics and Off-Road Vehicles*. Elsevier, Amsterdam The Netherlands New York NY U.S.A..
- Zuber, M.T., Head, J.W., Smith, D.E., et al., 2012. Constraints on the volatile distribution within Shackleton crater at the lunar South Pole. *Nature* 486, 378–381. doi:10.1038/nature11216.